Journal of King Saud University – Science 34 (2022) 102036

Contents lists available at ScienceDirect

Journal of King Saud University – Science

journal homepage: www.sciencedirect.com

Original article

Highly porous chitosan based magnetic polymeric nanocomposite (PNC) for the removal of radioactive, Cs(I) and Sr(II) ions from aqueous solution

Norah Alhokbany, Tansir Ahamad *, Saad M. Alshehri *

Department of Chemistry, King Saud University, Riyadh, Saudi Arabia

ARTICLE INFO

Article history:
Received 22 December 2021
Revised 11 April 2022
Accepted 12 April 2022
Available online 19 April 2022

Keywords:
Chitosan
Polymer nanocomposite
Radioactive
Adsorption

ABSTRACT

In the present study highly porous magnetic polymeric schiff base nanocomposite was fabricated using chitosan and 2-hydroxy-5-formylbenzoic acid in the presence of $NiFe_2O_4$. The analytical analysis (FTIR, TGA, XRD, BET, SEM, TEM and XPS) results support the successfully fabrication of $NiFe_2O_4$, polymeric matrix (PNC) and magnetic polymer nanocomposite ($NiFe_2O_4$@PNC). The surface area of $NiFe_2O_4$, and $NiFe_2O_4$@PNC was found to be 78.12, and 254 m^2/g for $NiFe_2O_4$, and $NiFe_2O_4$@ PNC respectively. The $NiFe_2O_4$@PNC used for the adsorption of radioactive metal ions, Cs(I) and Sr(II) and the adsorption capacity was found to 232.12 mg/g and 212.5 mg/g respectively. The interaction between the $NiFe_2O_4$@PNC and both the metal ions were determine using adsorption kinetics and adsorptions isotherms models, which support the pseudo-second order and Langmuir adsorption models take part. The regeneration results revealed that the $NiFe_2O_4$@PNC retain 94.1 and 92.0 % adsorption capacity after six cycles with Cs(I) and Sr(II). These results demonstrate that the fabricated $NiFe_2O_4$@PNC can be used as an advanced and efficient adsorbent for adsorbing toxic inorganic and organic pollutants from contaminated water.

1. Introduction

The demand for energy is increasing and energy sources are being reduced day by day to overcome these problems alternative energy sources such as nuclear power play a key role in meeting the energy demand. However, it was noticed that the, radioactive waste including U(VI), Cs(I), Sr(II), and many more ions were discharged into the natural environment without any form of treatment and resulting contaminate the water sources such as well, rivers, and sea (Tang et al., 2020; Munthali et al., 2015; Johansen et al., 2018). These radionuclides are toxic and have a long half-life. Long-term exposure to radionuclides can cause serious health problems such as cancer, infertility, neurological disorders, and birth death (Ivanets et al., 2020; Tachibana et al., 2020; Uematsu et al., 2020).

Therefore, the removal of these radioactive ions form an aqueous solution is urgently required. To date, various techniques such as liquid–liquid extraction, chemical precipitation, electrochemical treatment, membrane separation and adsorption have been used to remediate radioactive ions from contaminated water (Asgari et al., 2019; Liu and Wang, 2020; Sun et al., 2020; Wang et al., 2019). Besides these methods, adsorption and photocatalytic degradation are the most effective method for treating contaminated water, even for organic and inorganic pollutants, due to its low cost, ease of use and great accessibility (Ahamad et al., 2021; Ahamad et al., 2020; Ahamad et al., 2020; Ahamad et al., 2020). Several nano-systems have been used for the treatment of other toxic pollutants including dye, organic nutrients, antibiotics etc. from contaminated water (Kaur et al., 2021; Singh et al., 2022; Chakraborty et al., 2020; Chakraborty et al., 2021). Among these adsorbents polymeric resins and their nanocomposites have potential application due to their high surface area, tuning the selectivity and adsorption capacity with functional groups (Ghalami et al., 2019; Ogata et al., 2018; Bisla et al., 2020; Shi et al., 2020). However, the uses of these polymers as adsorbents are limited because of their separation and recovery after the adsorption of toxic pollutants is time consuming and costly.

Realizing these drawbacks, a series of investigations and study were exposed. Among them, the production of magnetic polymer nanocomposite and its use to remove toxic pollutants from aque-

* Corresponding authors.
E-mail addresses: nhokbany@KSU.EDU.SA (N. Alhokbany), tahamed@ksu.edu.sa (T. Ahamad), alshehri@ksu.edu.sa (S.M. Alshehri).
Peer review under responsibility of King Saud University.

Production and hosting by Elsevier

https://doi.org/10.1016/j.jksus.2022.102036
1018-3647/

ous solution is the most effective technique to solve the above problems. Previously, several magnetic nanocomposites have been used for the treatment of polluted aqueous solution. As we mention above that the porosity and the functional groups of the polymer nanocomposites can be tuned according to the desired applications. Therefore, in the present study, a highly porous magnetic polymeric nanocomposite was fabricated using chitosan, salicylaldehyde and $NiFe_2O_4$. The fabricated nanocomposite was well characterized and used for the adsorption of radioactive ions including Cs(I) and Sr(II) from aqueous solution. The interaction between the $NiFe_2O_4$@PNC and both the metal ions were determine using adsorption kinetics and adsorptions isotherms models. The regeneration results revealed that the $NiFe_2O_4$@PNC show promising adsorption capacity after six cycles with Cs(I) and Sr (II). The overall results, demonstrate that the fabricated $NiFe_2O_4$@-PNC can be used as an advanced and efficient adsorbent for adsorbing toxic inorganic and organic pollutants from contaminated water.

2. Experimental

2.1. Materials

Chitosan (low molecular weight < 50 kDa, degree of deacetylation 70–80%), 2-hydroxy-5-formylbenzoic acid, nickel(II) chloride hexahydrate ($NiCl_2{\cdot}6H_2O$), Iron(III) chloride hexahydrate ($FeCl_3{\cdot}6H_2O$), cesium nitrate, and strontium nitrate were purchased from Sigma Aldrich. Other chemicals were also used analytic grade without any purification. The magnetic $NiFe_2O_4$ nanoparticles were fabricated using co-precipitation method using ammonia solution.

2.2. Fabrication of the adsorbent ($NiFe_2O_4$@PNC)

To fabricate the magnetic nanocomposite 1 g of chitosan (Low molecular weight, <50 kDa) was dissolved in ethanol with help of dil. CH_3COOH, the emulsion was sonicated well and added 0.83 g of 2-hydroxy-5-formylbenzoic acid dissolved in ethanol to this solution slowly. The resulting mixture was stirred and heated at 60 °C for 1 h and then 0.5 g of $NiFe_2O_4$ nanoparticles was added and stirred and heated at 60 °C for 3 h. After that the pH of the solution was neutralized using aqueous NaOH solution and resulting yellow precipitate of $NiFe_2O_4$@PNC nanocomposite was filtered and washed with distilled water and separated with an extranet magnate and dried and storage in vacuum for further characterization and used. The details of characterization such as FTIR, TGA, XRD, BET, SEM, TEM, XPS and adsorption assay are given in supporting information.

3. Results and discussion

The magnetic adsorbent was fabricated using $NiFe_2O_4$ nanoparticles embedded into chitosan and 2-hydroxy-5-formylbenzoic acid based polymeric matrix. The polymer matrix was fabricated under acidic solution at 70 °C temperature and the synthetic route is illustrated in Fig. 1.

The FTIR spectra of the polymer (PNC), $NiFe_2O_4$ nanoparticles and the magnetic polymer nanocomposite ($NiFe_2O_4$@ PNC) are illustrated in Fig. 2(a). The FTIR spectra of the PNC shows several FTIR peaks at 3340–3481, 3060, 2945–2841, 1725, 1687, 1548, 1440 and 1178 cm^{-1} which assigned to –OH, =C–H, C–H, C=N, C=C, C-O, C-N stretching vibration, respectively (Shanavas et al., 2021). While in the case of the $NiFe_2O_4$@PNC the broadness of the O–H region was increased and additional peaks at 1665 cm^{-1} was observed due to presence of OH groups on the surface of $NiFe_2O_4$. Additionally, two peaks at 549 and 614 cm^{-1} were assigned to the Ni-O and Fe-O of the spinal structure of $NiFe_2O_4$. TGA curves of the polymer, $NiFe_2O_4$ and the $NiFe_2O_4$@PNC were recorded under the flow of air and recorded from room temperature to the 900 °C and the results are illustrated in Fig. 2(b). In the case of pure $NiFe_2O_4$ only 3.5 % weight loss was noticed and this may be due to the loss of adsorbed O–H groups up to 200 °C. However, in the case of the PNC and the $NiFe_2O_4$@PNC, the weight loss up to 200 °C were found to be 5.80% and 4.81 % respectively. The main degradation was carried out in second and third stages, the second stage, between 200 and 325 °C, and in this stage about 35.67 and 30.34 % weight loss was noticed. Moreover, the third degradation stage in the case of polymer is also fast and completely decomposed at 600 °C, while in the case of the $NiFe_2O_4$@PNC, he residue weight was found to be 24.88 %, due to the presence of the metal oxide (Ubaidullah et al., 2021; Alshehri et al., 2016). The crystalline nature and the purity of the $NiFe_2O_4$ nanoparticles and $NiFe_2O_4$@PNC was determined using X-ray diffraction patterns analysis. As shown in Fig. 2(c), the XRD results of the pure $NiFe_2O_4$ nanoparticles show the diffraction peaks at 2Θ = 29.95, 35.45, 37.50, 43.05, 53.65°, 56.89 and 62.89 with crystal planes (220), (311), (222), (400), (422), (511) and (440) respectively and support the spinel structure of $NiFe_2O_4$ (JCPDF-74-2061) (Gao et al., 2020; Lu et al., 2021). The XRD spectra of the $NiFe_2O_4$@PNC shows similar diffraction peaks without changing their position, however the peaks become broad and less instance, this is because the polymer is monocrystalline in nature (Al-Enizi et al., 2018). These outcomes additionally support the formation of the $NiFe_2O_4$ and maintain its originality in the $NiFe_2O_4$@-PNC. The porosity and the surface area of the $NiFe_2O_4$, and $NiFe_2O_4$@ PNC was determined using N_2 adsorption–desorption isotherm. As shown in Fig. 2(d), the CSRs and $NiFe_2O_4$@ PNC show the mesoporous nature with the type IV hysteresis loop based on IUPAC classification (Ahamad et al., 2021). The surface area was determine using BET and observed about to be 78.12, and 254 m^2/g for $NiFe_2O_4$, and $NiFe_2O_4$@ PNC respectively. Additionally, the average pore volume was calculated using the BJH equation and in the case of the $NiFe_2O_4$, and $NiFe_2O_4$@PNC it was found to be 15 nm, and 28 nm respectively.

The morphology of the $NiFe_2O_4$ and $NiFe_2O_4$@ PNC was determine using SEM images, as shown in Fig. 3(a) (b), the SEM image display that the $NiFe_2O_4$ nanoparticles are spherical shape with a particles size range of 8–12 nm. The SEM image of the $NiFe_2O_4$@-PNC revealed that the nanoparticles are embedded uniformly into the polymer matrix of PNC. However, the presence of the polymer in nanocomposites reduces the aggregation of the magnetic nanoparticles. Further, the morphology of the $NiFe_2O_4$@PNC was determined using TEM technique as shown in Fig. 3(c). And the results revealed that the surface of the nanoparticles was smooth spherical shape and uniform in size with average diameter about 9 nm and embedded in to the polymer matrix. The HRTEM image of the nanocomposites display the crystalline nature of the magnetic $NiFe_2O_4$ nanoparticles and the lattice fringes was clearly identified with d- spacing 2.96 nm and 4.87 nm due to the (220) and (111) plane of the $NiFe_2O_4$ (Pang et al., 2021; Ren et al., 2014) as displayed in Fig. 3(d).

The present of elements on the surface and their oxidation were determined using X-ray photoelectron spectroscopy (XPS). The XPS spectrum of the $NiFe_2O_4$@PNC displays the presence of C, N, O, Ni, and Fe elements without any impurities, however there is no peaks for Ni, and Fe were found in the XPS spectra of NPC, as illustrated in Fig. 4(a). The high-resolution spectra of the Fe 2p is illustrated in Fig. 4(b) and split into two central peaks and appear at binding energy of around 711.14 and 725.23 eV, due to Fe $2p_{3/2}$ and Fe $2p_{1/2}$ respectively. While, another peak at 718.43 eV is assigned to the satellite pack belonging to the Fe $2p_{3/2}$ and support the presence of Fe^{3+} ions. The Ni 2p spectrum of the nanocomposite display

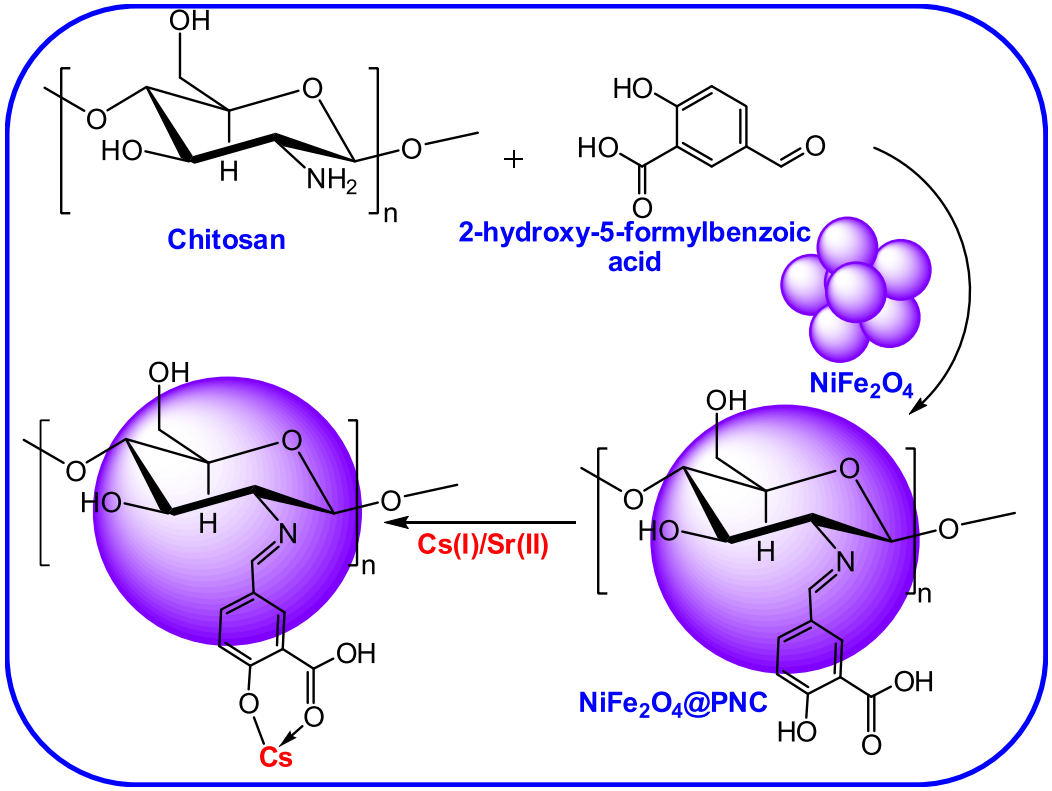

Fig. 1. The synthesis routes for the synthesis of $NiFe_2O_4$@PNC.

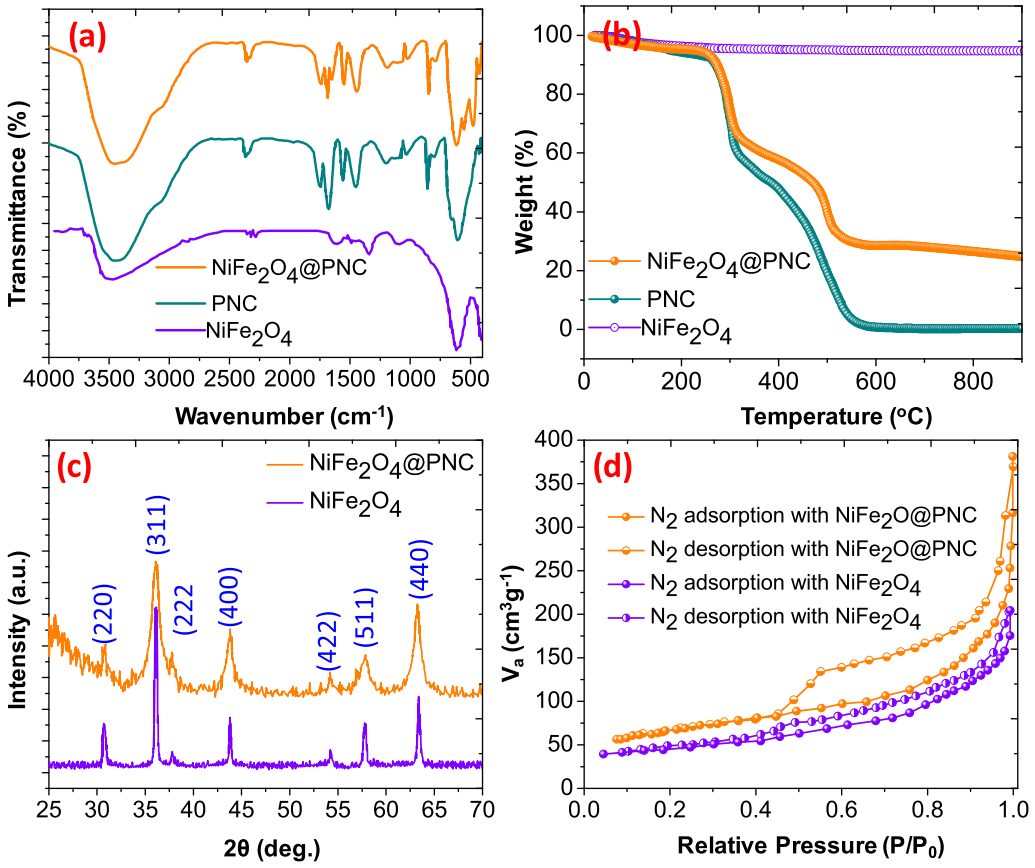

Fig. 2. (a) FTIR spectra of $NiFe_2O_4$, PNC and $NiFe_2O_4$@PNC (b) TGA/DTA curves of $NiFe_2O_4$, PNC and $NiFe_2O_4$@PNC (c) XRD of $NiFe_2O_4$, and $NiFe_2O_4$@PNC (d) N_2 adsorption and desorption of $NiFe_2O_4$, and $NiFe_2O_4$@PNC.

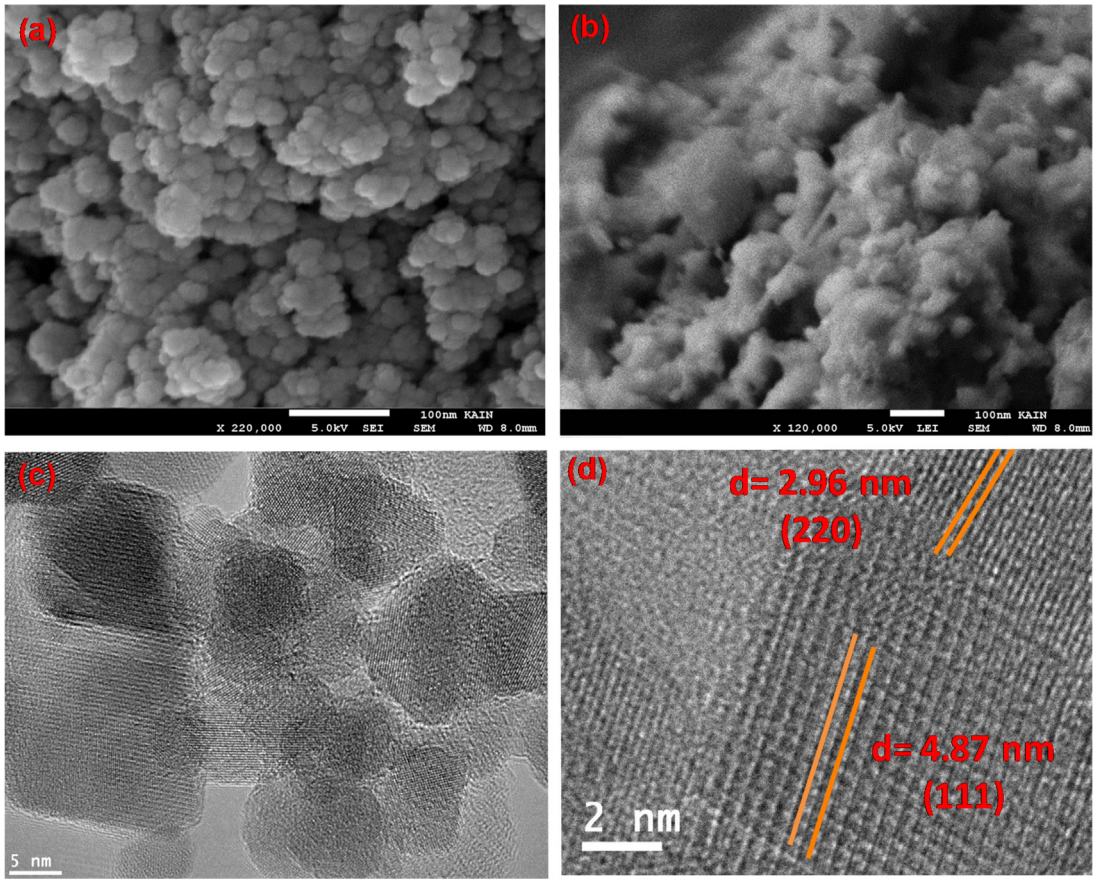

Fig. 3. (a) SEM image of $NiFe_2O_4$ (b) SEM image of $NiFe_2O_4$@PNC (a) TEM image of $NiFe_2O_4$@PNC (d) HRTEM image of $NiFe_2O_4$@PNC.

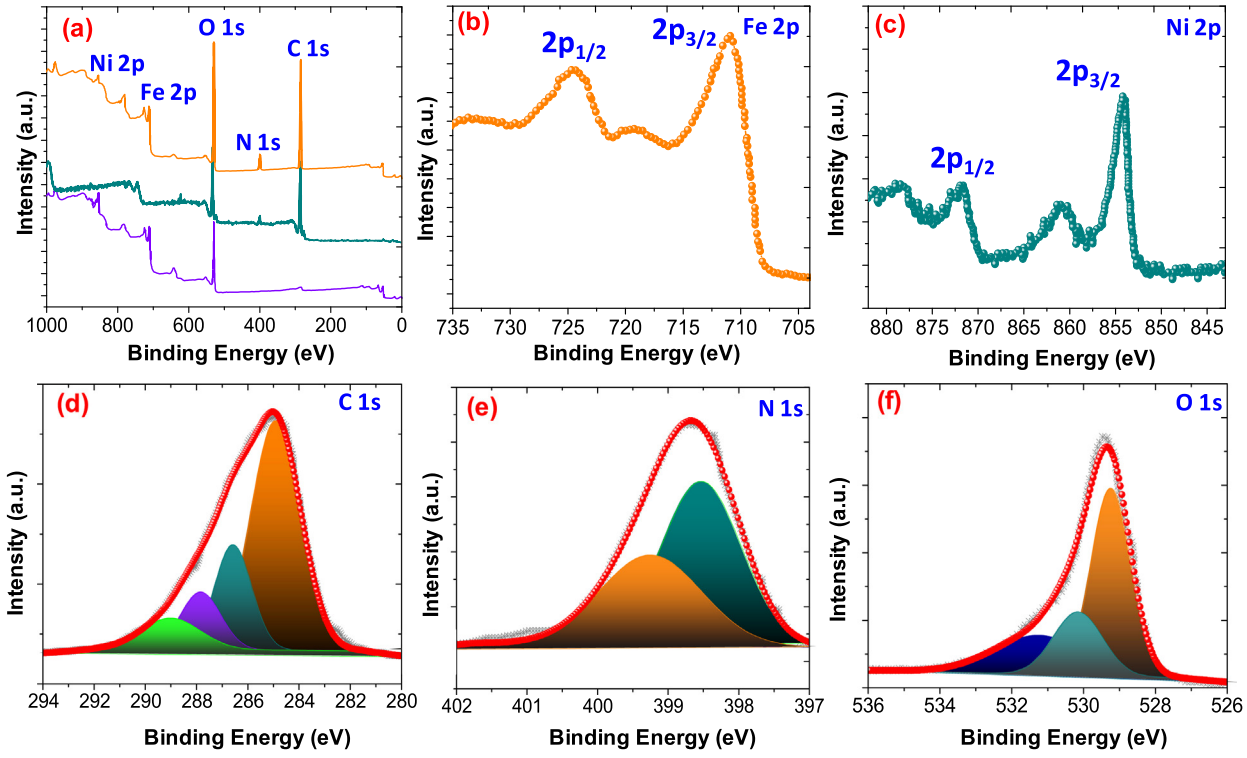

Fig. 4. (a) A wide XPS spectra for $NiFe_2O_4$, PNC and $NiFe_2O_4$@PNC (b) Fe2p, (c) Ni 2p (d) C 1s, (e) N1s (f) O1s.

two core peaks with two satellite peaks, the core peaks appear at binding energy 855.74 eV and 873.2 eV and assigned to the Ni $2p_{3/2}$ and Ni $2p_{1/2,}$ respectively as displayed in Fig. 4(c). While the peaks at 862.1 and 880.7 eV appear due to the satellites peak of Ni $2p_{3/2}$ and Ni $2p_{1/2}$, respectively and support the existence of Ni^{2+} in the nanocomposite. These results support that the nanoparticles and the nanocomposite contain Ni^{2+} and Fe^{3+} and their atomic ratio was found to be 1:2, being consistent with the stoichiometry of $NiFe_2O_4$.

As shown in Fig. 4(d), the high resolution spectra of the C 1s was deconvoluted into four peaks and appear the binding energy at 283.72 eV, 285.82 eV, 286.85 eV and 287.92 eV which were allocated to the C–C/C=C, C=O, C=N and C-O respectively(Ahamad et al., 2021). The XPS spectrum of N1s was split into two main pecks and appeared at binding energy of 398.60 eV, and 399.024 eV and support the formation of the C=N, - and –NH functional groups in the polymer matrix respectively as shown in Fig. 4 (e). As displayed in Fig. 4(f), the O1s spectrum was deconvoluted into three peaks and appear at binding energy of 529.29 eV, 530.31 eV and 531.85 eV which were assigned to Fe-O/Ni-O, C-O/C=O, and O–H respectively.

The magnetic properties of the nanocomposite and $NiFe_2O_4$ nanoparticles were recorded using VSM analysis at room temperature and the observed magnetic curves were illustrated in Fig. 5(a). It was noticed that the saturation magnetization of the pure magnetic $NiFe_2O_4$ nanoparticles was reduced from 46.84 emu/g to 32.02 emu/g after the formation of the $NiFe_2O_4$@PNC. This may be due to weight of the nonmagnetic polymer, however the superparamagnetic properties of the $NiFe_2O_4$ retained in the nanocomposite and can be simply removed from the contaminated solution using an external magnate (Naushad et al., 2019). The zero-charge point of the $NiFe_2O_4$ and $NiFe_2O_4$@PNC was determined illustrated in Fig. 5(b). It was noticed that the zero-charge point was found at pH 7.12 and 6.54 for $NiFe_2O_4$ and $NiFe_2O_4$@PNC respectively.

3.1. Batch adsorption studies

To determine the adsorption capacity and the optimum adsorption conditions, the adsorption process was carried out by changing several factors such as pH, initial concentration, time and temperature (Pathania et al., 2017). The pH of aqueous solution is one of the main reason, which affect the adsorption capacity of the adsorbents. As shown in Fig. 6(a), when the pH of the solution was improved form 2 to 7 the adsorption of Cs(I) and Sr(II) was increased and the absorption capacity of $NiFe_2O_4$@PNC at pH 7 were found to be 232.5, and 212.2 mg/g respectively.

On the other hand, when the pH was improved more than 7 the adsorption of both the ions was slightly declined and at pH 10 the adsorption capacity was found to be 222.4 and 203.5 mg/g against Cs(I) and Sr(II) respectively at room temperature. This may be because, at lower pH the surface of the $NiFe_2O_4$@PNC was protonated resulting decreased the adsorption capacity. However, when the pH was more then 7, the metal ions were formed it corresponding hydroxides and reduced the adsorption capacity of the $NiFe_2O_4$@PNC at room temperature (Naushad et al., 2020). Based on these outcomes, the optimum pH was used 7 in all other adsorption experiment. The initial concentration of the Cs(I) and Sr(II) also affect the adsorption capacity of the $NiFe_2O_4$@PNC and the adsorption was run with a wide range of metal ions, from 5 mg/L to 300 mg/L were tested. It was observed, that when the initial concentrations of the Cs(I) and Sr(II) ions were increased form 5 mg/L to 100 mg/L the percentage adsorption and adsorption capacity was increased. However, when the initial concentration was further increased, up to 300 mg/L minor increment were noticed and the adsorption capacity and were found to be 249.75, and 229.70 mg/g against Cs(I) and Sr(II) respectively at room temperature and at pH 7. These outcomes support that the as the initial concentrations of the metal ions were increased the adsorption site of the adsorbent was decreased and at 100 mg/L concentration most of the active sites were occupied with the metal ions. Therefore, the initial concentration 100 mg/L of Cs(I) and Sr(II) were used as the optimum initial concentration. To determine the effect of the contact time the adsorption process, the experiment was carried out with different contact time range, from 5 to 200 min, at pH 7, initial concentration 100 mg/L and at room temperature and results are illustrated in Fig. 6(c). It was observed that when the time was increased form 5 min to 30 min the adsorption of all the metal ions were increased sharply and after 30 min the adsorption capacity of $NiFe_2O_4$@PNC was found 240.21 and 219.92 mg/g and the equilibrium was occurring after 60, min for both the Cs (II) and Sr(II) ions. To find out the optimum temperature for the adsorption of both the metal ions Cs(I) and Sr(II) ions, the experiments were carried out at 25, 35, 40, 45 and 50 °C. and the adsorption capacities were found to be 232.12, 230.4, 227.5 and 225.21 mg/g for Cs(I), while in the case of Sr(II) were found to be 212.5, 211.6, 207, 205.2 and 200.1 respectively as illustrated in Fig. 6(d). These outcomes revealed that the adsorption of both metal ions were decreased with increasing the temperature of the solution.

3.1.1. Adsorption kinetics and isotherm

The role of the adoption time with the interaction between the metal ions and the $NiFe_2O_4$@PNC, and the adsorption kinetics

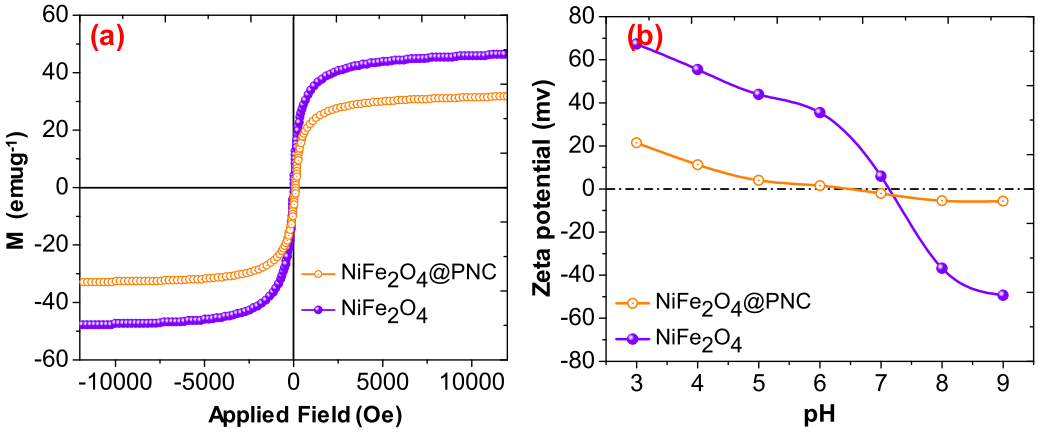

Fig. 5. (a) Magnetic measurements and (b) Zeta potential of $NiFe_2O_4$, and $NiFe_2O_4$@PNC.

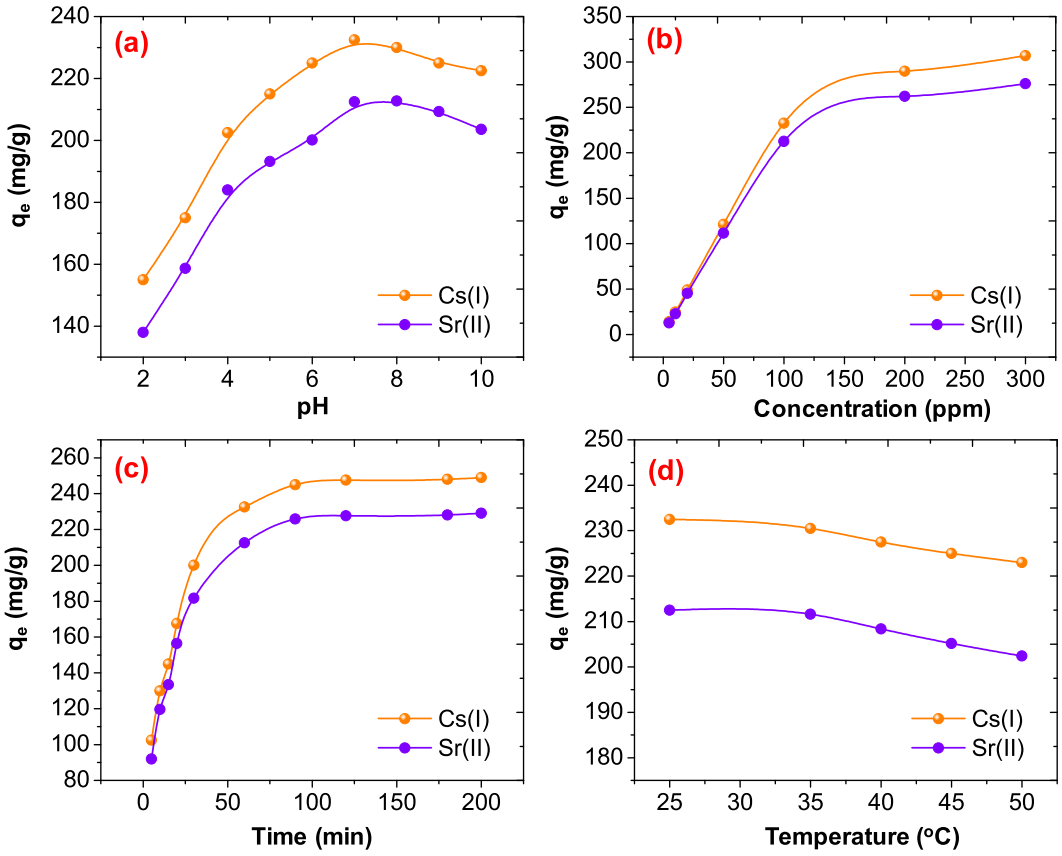

Fig. 6. Effect of (a) pH (b) concentration (c) time and (d) temperature on the adsorption of Cs(I) and Sr(II) onto $NiFe_2O_4$@PNC.

determine the rate at which the adsorption occurs. The kinetic results and equilibrium adsorption of both the metal ions are showed in Fig. 7(a) and 7(b), and the parameters were concise in Table 1.

The kinetics parameters were determine using nonlinear model of pseudo-first-order (PFO), pseudo-second-order (PSO) and intra-particle diffusion model (IPD) at room temperature. Details of these models are given in supplementary material. It was seen that the adsorption data of both the metal ions were fitted well with and follow the PSO reaction kinetics model. This is because in the case of pseudo-second-order model the correlation coefficient (R^2) was found to be 0.9914 while it was found 0.9329 and 0.8232 for pseudo-first-order, and Intra-particle respectively during the adsorption of Cs(I) ions. While in the case of Sr(II) the R^2 was found to be 0.9854 while it was found 0.9387 and 0.8432 for PSO, PFO and Intra-particle respectively. These outcomes revealed that the pseudo-second-order kinetic model support the chemisorption process for the adsorption of Cs(I) and Sr(II).

The adsorption isotherm supports the find out the interaction between the metal ions and the $NiFe_2O_4$@PNC at the equilibrium concentration of the Cs(I) and Sr(II) ions and the amount of adsorbate. Adsorption isotherm was carried out using the Langmuir, Freundlich, and Temkin isotherm model. Their details are given in supplementary material. The adsorption isotherm parameters for Langmuir, Freundlich, and Temkin isotherm model are summarized in Table 2. The nonlinear fitting of the experimental data is illustrated Fig. 7(a) and 7(b), it was noticed that the higher correlation coefficient (R^2) of Langmuir isotherm was fitted well batter then that of the Freundlich, and Temkin models and their value was found to be 0.9854, 0.9306, and 0.9365 respectively during the adsorption of Cs(I). While with Sr(II), the value of R^2 was found to be 0.9792 in Langmuir isotherm model. These outcomes indicate that the adsorption of both the metal ions were carried out via monolayer homogeneous adsorption and the maximum adsorption capacity were found to be 242.21, and 214.23 mg/g, with the Cs(I) and Sr(II) respectively and the comparison with other adsorbents is summarised supporting table S-1.

3.1.2. Adsorption thermodynamics

To determine the effect of temperature during the adsorption of the Cs(I) and Sr(II) on $NiFe_2O_4$@PNC the temperature was changed from 25 to 50 under optimum condition. The results revealed that the adsorption capacities of $NiFe_2O_4$@PNC were as the temperature was increased. To further determine the thermodynamics parameters such as entropy change (ΔS), free energy change (ΔG) and enthalpy change (ΔH), Van't Hoff equation has been used as the details are given in supporting information. The value of the ΔS, ΔH were calculated with the liner fitting of Van't Hoff as illustrated in figure-8(a). It was noticed that the positive values of the ΔS and ΔH support that the adsorption of both the metal ions were endothermic and the positive value of ΔG support the spontaneous adsorption.

3.1.3. Regeneration of $NiFe_2O_4$@PNC

Regeneration of adsorbents is an important parameter from application point of view. Thus, the regeneration was carried out with six cycles and $NiFe_2O_4$@PNC was washed after each adsorption cycles using dil HCl and deionised to use for next cycles to economize the production cost (Asgari et al., 2020; Mohammadabadi and Javanbakht, 2020). As shown in Fig. 8(b), it was noticed that the adsorption capacity of the $NiFe_2O_4$@PNC was found to be 94.1% and 92.0 % after six cycles, which suggests that as-fabricated $NiFe_2O_4$@PNC is an excellent cost-effective

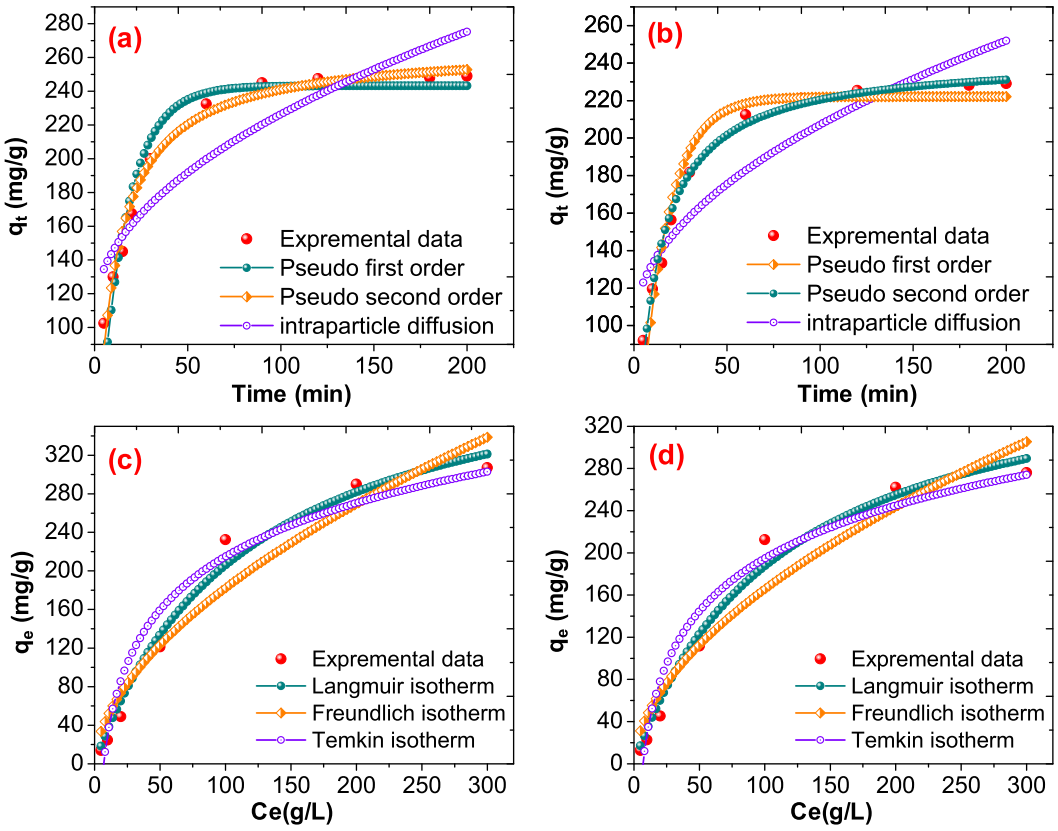

Fig. 7. (a) Adsorption kinetics of Cs(I) (b) Adsorption kinetics of Sr(II) (c) Adsorption isotherms for the adsorption of Cs(I) (d) Adsorption isotherms for the adsorption of Sr(II) on $NiFe_2O_4$@PNC.

Table 1
Adsorption kinetic parameters for the adsorption of Cs(I) and Sr(II) on $NiFe_2O_4$@PNC.

Metal Ions	Kinetic models	Parameters	
Cs(I)	***PFO model***	q_e (mg·g^{-1})	243.20
		k_1 (min^{-1})	0.6758
		R^2	0.9329
	PSO model	q_e (mg·g^{-1})	265.81
		k_2 (g·mg^{-1}·min^{-1})	3.64x10^{-4}
		R^2	0.9914
	Intra-particle diffusion	C	10.8
		K_{dif} (mg g^{-1} min$^{-1/2}$)	11.81
		R^2	0.8232
Cd(II)	***PFO model***	q_e (mg·g^{-1})	222.10
		k_1 (min^{-1})	0.0683
		R^2	0.9387
	PSO model	q_e (mg·g^{-1})	242.95
		k_2 (g·mg^{-1}·min^{-1})	4.01X10^{-4}
		R^2	0.9854
	Intra-particle diffusion	C	9.87
		K_{dif} (mg g^{-1} min$^{-1/2}$)	1083
		R^2	0.8432

Table 2
Adsorption isotherm parameters for the adsorption of Cs(I) and Sr(II) on $NiFe_2O_4$@PNC.

Metal Ions	Isotherm models	Parameters	
Cs(I)	***Langmuir model***	q_m (mg·g^{-1})	242.21
		K_L (L·mg^{-1})	0.0085
		R^2	0.9854,
	Freundlich model	K_f (mg$^{1-1/n}$·L$^{1/n}$·g^{-1})	13.57
		n	1.77
		R^2	0.9306,
	Tamkin model	K_t (L/gm)	0.1462
		B_t	80.08
		R^2	0.9365
Sr (II)	***Langmuir model***	q_m (mg·g^{-1})	214.23
		K_L (L·mg^{-1})	0.0089
		R^2	0.9792
	Freundlich model	K_f (mg$^{1-1/n}$·L$^{1/n}$·g^{-1})	17.76
		n	1.796
		R^2	0.9551
	Tamkin model	K_t (L/gm)	0.148
		B_t	72.24
		R^2	0.9591

adsorbent for the adsorption of radioactive Cs(I) and Sr(II) form polluted aqueous solution.

3.1.4. Adsorption mechanism

To determine the adsorption mechanism for the adsorption of Cs(I) and Sr(II) onto $NiFe_2O_4$@PNC FTIR and XPS were used. As shown in Fig. 8(c), the FTIR spectra after the adsorbent of Cs(I) and Sr(II) were compared with the spectra of fresh $NiFe_2O_4$@PNC and used $NiFe_2O_4$@PNC after 2 cycles. It was noticed that after the adsorption of Cs(I) and Sr(II), the FTIR band at 1687 cm^{-1} was shifted to lower frequency and observed at 1644 and 1641 cm^{-1} respectively, while after the desorption of the metal ions this peaks reached on its original position. These results support the coordination of metal ions with the C=N groups. The adsorption of Cs(I) and Sr(II) was further determine using XPS analysis and the results were illustrated in Fig. 8(d), the wild range XPS spectra of $NiFe_2O_4$@PNC-Cs(I) and $NiFe_2O_4$@PNC-Sr(II) show the presence of Cs(I) and Sr(II) ions at binding energy about 423–737 eV and 135.5 eV respectively. Moreover, the XPS spectrum of adsorbent $NiFe_2O_4$@PNC after 2 cycles shown that there is no Cs (I) and Sr(II) elements are not presence on its surface and desorb

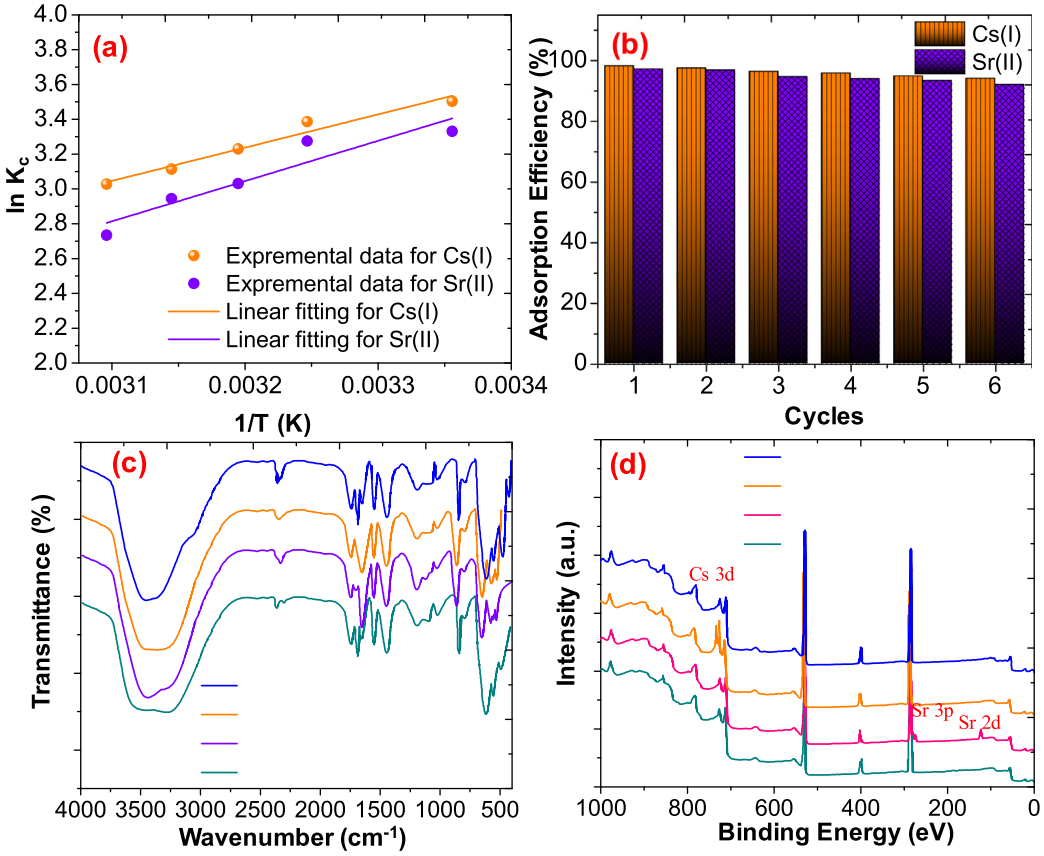

Fig. 8. (a) adsorption thermodynamic of Cs(I) and Sr(II) over $NiFe_2O_4$@PNC (d) regeneration behaviour of $NiFe_2O_4$@PNC (c) FTIR spectra of $NiFe_2O_4$@PNC after adsorption and desorption (d) XPS analysis of $NiFe_2O_4$@PNC after adsorption and desorption.

completely and no change in the chemical composites of the adsorbent was notices after regeneration.

4. Conclusions

In the present study, we have prepared $NiFe_2O_4$, PNC and $NiFe_2O_4$@PNC, and all the prepared compounds were well characterised using several analytical techniques. The adsorption of Cs(I) and Sr (II) on $NiFe_2O_4$@PNC were studied and the adsorption capacity was found to 232.12 mg/g and 212.5 mg/g respectively. The adsorption kinetics and adsorptions isotherms models support the pseudo-second order and Langmuir adsorption models respectively. The regeneration was carried out with the help of dil HCl and the results revealed that the $NiFe_2O_4$@PNC retains 94.1 and 92.0 % adsorption capacity after six cycles with Cs(I) and Sr(II). The interaction between the metal and the adsorbent was discussed and the overall out comes suggest that the fabricated adsorbent can be used for effective removal of radioactive models Cs(I) and Sr(II) ions form contaminated water.

Declaration of Competing Interest

The authors declare that they have no known competing financial interests or personal relationships that could have appeared to influence the work reported in this paper.

Acknowledgement

The authors extend their appreciation to the King Saud University, Saudi Arabia for funding this research work through the project number RSP-2021/29.

Appendix A. Supplementary data

Supplementary data to this article can be found online at https://doi.org/10.1016/j.jksus.2022.102036.

References

Tang, X., Zhou, L., Le, Z., Wang, Y., Liu, Z., Huang, G., Adesina, A.A., 2020. Preparation of porous chitosan/carboxylated carbon nanotube composite aerogels for the efficient removal of uranium(VI) from aqueous solution. Int. J. Biol. Macromol. 160, 1000–1008.
Munthali, M.W., Johan, E., Aono, H., Matsue, N., 2015. Cs+ and Sr2+ adsorption selectivity of zeolites in relation to radioactive decontamination. J. Asian Ceram. Soc. 3 (3), 245–250.
Johansen, M.P., Prentice, E., Cresswell, T., Howell, N., 2018. Initial data on adsorption of Cs and Sr to the surfaces of microplastics with biofilm. J. Environ. Radioact. 190–191, 130–133.
Ivanets, A., Milyutin, V., Shashkova, I., Kitikova, N., Nekrasova, N., Radkevich, A., 2020. Sorption of stable and radioactive Cs(I), Sr(II), Co(II) ions on Ti–Ca–Mg phosphates. J. Radioanal. Nucl. Chem. 324 (3), 1115–1123.
Tachibana, Y., Kalak, T., Nogami, M., Tanaka, M., 2020. Combined use of tannic acid-type organic composite adsorbents and ozone for simultaneous removal of various kinds of radionuclides in river water. Water Res. 182.
Uematsu, Y., Ogata, F., Saenjum, C., Nakamura, T., Kawasaki, N., 2020. Removing Sr (II) and Cs(I) from the aqueous phase using basil seed and elucidating the adsorption mechanism. Sustainability (Switzerland) 12 (7).
Asgari, P., Mousavi, S.H., Aghayan, H., Ghasemi, H., Yousefi, T., 2019. Nd-BTC metal-organic framework (MOF); synthesis, characterization and investigation on its adsorption behavior toward cesium and strontium ions. Microchem. J. 150.
Liu, X., Wang, J., 2020. Adsorptive removal of Sr2+ and Cs+ from aqueous solution by capacitive deionization. Environ. Sci. Pollut. Res.
Sun, H., Liu, Y., Lin, J., Yue, Z., Li, W., Jin, J., Sun, Q., Ai, Y., Feng, M., Huang, X., 2020. Highly selective recovery of lanthanides by using a layered vanadate with acid and radiation resistance. Angew. Chem. – Int. Ed. 59 (5), 1878–1883.
Wang, K.Y., Ding, D., Sun, M., Cheng, L., Wang, C., 2019. Effective and rapid adsorption of Sr2+ ions by a hydrated pentasodium cluster templated zinc thiostannate. Inorg. Chem. 58 (15), 10184–10193.

Ahamad, T., Naushad, M., Alshehri, S.M., 2021. Analysis of degradation pathways and intermediates products for ciprofloxacin using a highly porous photocatalyst. Chem. Eng. J. 417, 127969.
Ahamad, T., Naushad, M., Alzaharani, Y., Alshehri, S.M., 2020. Photocatalytic degradation of bisphenol-A with g-C3N4/MoS2-PANI nanocomposite: kinetics, main active species, intermediates and pathways. J. Mol. Liq. 311, 113339.
Ahamad, T., Naushad, M., Al-Saeedi, S.I., Almotairi, S., Alshehri, S.M., 2020. Fabrication of MoS2/ZnS embedded in N/S doped carbon for the photocatalytic degradation of pesticide. Mater. Lett. 263, 127271.
Ahamad, T., Naushad, M., Al-Shahrani, T., Al-hokbany, N., Alshehri, S.M., 2020. Preparation of chitosan based magnetic nanocomposite for tetracycline adsorption: kinetic and thermodynamic studies. Int. J. Biol. Macromol. 147, 258–267.
Kaur, N., Khunger, A., Wallen, S.L., Kaushik, A., Chaudhary, G.R., Varma, R.S., 2021. Advanced green analytical chemistry for environmental pesticide detection. Curr. Opin. Green Sustainable Chem. 30, 100488.
Singh, P., Kaur, N., Khunger, A., Kaur, G., Kumar, S., Kaushik, A., Chaudhary, G.R., 2022. Green-monodispersed Pd-nanoparticles for improved mitigation of pathogens and environmental pollutant. Mater. Today Commun. 30, 103106.
Chakraborty, U., Bhanjana, G., Adam, J., Mishra, Y.K., Kaur, G., Chaudhary, G.R., Kaushik, A., 2020. A flower-like ZnO–Ag2O nanocomposite for label and mediator free direct sensing of dinitrotoluene. RSC Adv. 10 (46), 27764–27774.
Chakraborty, U., Bhanjana, G., Kannu, N., Kaur, R., Sharma, G., Kaur, A., Kaushik, G.R. C., 2021. Microwave-assisted assembly of Ag2O-ZnO composite nanocones for electrochemical detection of 4-Nitrophenol and assessment of their photocatalytic activity towards degradation of 4-Nitrophenol and Methylene blue dye. J. Hazard. Mater. 416, 125771.
Ghalami, Z., Ghoulipour, V., Khanchi, A., 2019. Highly efficient capturing and adsorption of cesium and strontium ions from aqueous solution by porous organic cage: a combined experimental and theoretical study. Appl. Surf. Sci. 471, 726–732.
Ogata, F., Nagai, N., Ueta, E., Nakamura, T., Kawasaki, N., 2018. Biomass potential of virgin and calcined tapioca (cassava starch) for the removal of Sr(II) and Cs(I) from aqueous solutions. Chem. Pharm. Bull. 66 (3), 295–302.
Bisla, V., Rattan, G., Singhal, S., Kaushik, A., 2020. Green and novel adsorbent from rice straw extracted cellulose for efficient adsorption of Hg (II) ions in an aqueous medium. Int. J. Biol. Macromol. 161, 194–203.
Shi, X., Qiao, Y., An, X., Tian, Y., Zhou, H., 2020. High-capacity adsorption of Cr(VI) by lignin-based composite: characterization, performance and mechanism. Int. J. Biol. Macromol. 159, 839–849.
Shanavas, S., Ahamad, T., Alshehri, S.M., Acevedo, R., Anbarasan, P.M., 2021. A facile microwave route for fabrication of NiO/rGO hybrid sensor with efficient CO2 and acetone gas sensing performance using clad modified fiber optic method. Optik 226, 165970.
Ubaidullah, M., Al-Enizi, A.M., Ahamad, T., Shaikh, S.F., Al-Abdrabalnabi, M.A., Samdani, M.S., Kumar, D., Alam, M.A., Khan, M., 2021. Fabrication of highly porous N-doped mesoporous carbon using waste polyethylene terephthalate bottle-based MOF-5 for high performance supercapacitor. J. Storage Mater. 33, 102125.
Alshehri, S.M., Aldalbahi, A., Al-hajji, A.B., Chaudhary, A.A., Panhuis, M.I.H., Alhokbany, N., Ahamad, T., 2016. Development of carboxymethyl cellulose-based hydrogel and nanosilver composite as antimicrobial agents for UTI pathogens. Carbohydr. Polym. 138, 229–236.
Gao, X., Bi, J., Wang, W., Liu, H., Chen, Y., Hao, X., Sun, X., Liu, R., 2020. Morphology-controllable synthesis of NiFe2O4 growing on graphene nanosheets as advanced electrode material for high performance supercapacitors. J. Alloy. Compd. 826, 154088.
Lu, Y.-B., Wang, H.-C., She, X.-Y., Huang, D., Yang, Y.-X., Gao, X., Zhu, Z.-M., Liu, X.-X., Xie, Z., 2021. A novel preparation of GO/NiFe2O4/TiO2 nanorod arrays with enhanced photocatalytic activity for removing unsymmetrical dimethylhydrazine from water. Mater. Sci. Semicond. Process. 121, 105448.
Al-Enizi, A.M., Ahamad, T., Al-hajji, A.B., Ahmed, J., Chaudhary, A.A., Alshehri, S.M., 2018. Cellulose gum and copper nanoparticles based hydrogel as antimicrobial agents against urinary tract infection (UTI) pathogens. Int. J. Biol. Macromol. 109, 803–809.
Ahamad, T., Aldalbahi, A., Alshehri, S.M., Alotaibi, S., Alzahly, S., Wang, Z.-B., Feng, P. X., 2021. Enhanced photovoltaic performance of dye-sensitized solar cells based Ag2O doped BiFeO3 hetrostructures. Sol. Energy 220, 758–765.
Pang, B., Zhang, M., Zhou, C., Dong, H., Ma, S., Feng, J., Chen, Y., Yu, L., Dong, L., 2021. Heterogeneous FeNi3/NiFe2O4 nanoparticles with modified graphene as electrocatalysts for high performance dye-sensitized solar cells. Chem. Eng. J. 405, 126944.
Ren, A., Liu, C., Hong, Y., Shi, W., Lin, S., Li, P., 2014. Enhanced visible-light-driven photocatalytic activity for antibiotic degradation using magnetic NiFe2O4/Bi2O3 heterostructures. Chem. Eng. J. 258, 301–308.
Naushad, M., Ahamad, T., Al-Ghanim, K.A., Al-Muhtaseb, A.A.H., Eldesoky, G.E., Khan, A.A., 2019. A highly porous nanocomposite (Fe3O4@BFR) for the removal of toxic Cd(II) ions from aqueous environment: adsorption modelling and regeneration study. Compos. B Eng. 172, 179–185.
Pathania, D., Sharma, S., Singh, P., 2017. Removal of methylene blue by adsorption onto activated carbon developed from Ficus carica bast. Arabian J. Chem. 10, S1445–S1451.
Naushad, M., Ahamad, T., Al-Sheetan, K.M., 2020. Development of a polymeric nanocomposite as a high performance adsorbent for Pb(II) removal from water medium: equilibrium, kinetic and antimicrobial activity. J. Hazard. Mater. 407, 124816.
Asgari, E., Sheikhmohammadi, A., Yeganeh, J., 2020. Application of the Fe3O4-chitosan nano-adsorbent for the adsorption of metronidazole from wastewater: optimization, kinetic, thermodynamic and equilibrium studies. Int. J. Biol. Macromol. 164, 694–706.
Mohammadabadi, S.I., Javanbakht, V., 2020. Lignin extraction from barley straw using ultrasound-assisted treatment method for a lignin-based biocomposite preparation with remarkable adsorption capacity for heavy metal. Int. J. Biol. Macromol. 164, 1133–1148.